RESEARCH   **Open Access**

Polyethylenimine-CO$_2$ adduct templated CaCO$_3$ nanoparticles as anticancer drug carrier

Wenli Luo, Zhaojian Li, Ling Zhang[*] and Xingyi Xie[*]

*Correspondence:
zhangling83@scu.edu.cn;
xiexingyi@scu.edu.cn

College of Polymer Science
and Engineering, Sichuan
University, Chengdu 610065,
Sichuan, People's Republic
of China

Abstract

Background: Due to their porous structure and capability to degrade under acidic conditions, CaCO$_3$ nanoparticles in vaterite form can be used as carriers to effectively deliver drugs to low-pH sites such as tumors. The usually used intravenous administration requires long-term vaterite phase and colloidal stability for storage and blood circulation. While passive accumulation in tumors can be achieved via the enhanced permeation and retention effect, active accumulation requires reactive groups on vaterite nanoparticles to conjugate targeting molecules. Both requirements are hard to achieve in one simple and economical vaterite formulation. Herein, we used polyethylenimine (PEI)-based CO$_2$ adduct as both a CO$_2$ source and a template for vaterite mineralization to generate PEI-CO$_2$@CaCO$_3$ colloidal particles, with reactive amino groups from the PEI template.

Results: The obtained nanoparticles with a hydrodynamic diameter of 200–300 nm have a vaterite phase and colloidal stability in an aqueous solution for over 8 months. These nanoparticles could effectively load anticancer drug doxorubicin via coprecipitation and be surface-modified with polyethylene glycol (PEG) and folic acid for long-term blood circulation and tumor targeting purposes, respectively. After being endocytosed, the PEI-CO$_2$ adduct accelerates the dissolution of drug-loaded nanoparticles to generate CO$_2$ bubbles to break the lysosomes, leading to rapid doxorubicin delivery inside tumor cells. The degradation of PEI-CO$_2$ in the CaCO$_3$ nanoparticles could also release PEI and CO$_2$ and may contribute to the disruption of normal cellular functions. As a result, the drug-loaded PEI-CO$_2$@CaCO$_3$ nanoparticles strongly suppressed tumor growth in mice with HeLa tumor xenografts.

Conclusions: A new and effective vaterite drug carrier for anticancer therapy has been developed using PEI-CO$_2$ adduct as both a CO$_2$ source and vaterite template for CaCO$_3$ mineralization. This delivery system illustrates an application of CO$_2$ generation materials in drug delivery and has the potential for further development.

Keywords: CaCO$_3$ nanoparticles, CO$_2$ adduct, Polyethyleneimine, pH-sensitive, Antitumor drug delivery

Introduction

As the most abundant biomineral found in skeletons of most invertebrates and eggshells of some vertebrates, calcium carbonate ($CaCO_3$) has been widely used in biomedical engineering, such as in fillers for bone implants (Unger et al. 2022) and as drug carriers for targeted delivery (Popova et al. 2021; Som et al. 2016). Calcite, aragonite, and vaterite are anhydrous polymorphs of calcium carbonate, whereas amorphous calcium carbonate (ACC), ikaite, and monohydrocalcite belong to the hydrated forms (Morse et al. 2007). Among them, vaterite with crystals of typical nano sizes attracts the most attention due to its spherical shape and porous structure, although it might recrystallize in water to non-porous calcite within several hours (Volodkin et al. 2004). The ACC is the least stable crystal form and can dissolute in water, despite its nanospherical structure (Zhao et al. 2015). The most stable form of $CaCO_3$ is calcite. The in vivo lysosomal acidic environment cannot effectively decompose it to release the encapsulated drugs (Wang et al. 2018), limiting its application for drug delivery systems. On the contrary, vaterite is a pH-sensitive porous carrier with tumor-triggered intracellular drug release (Wang et al. 2018; Min et al. 2015). In addition, vaterite with good biocompatibility can encapsulate some fragile biomolecules (Balabushevich et al. 2015; Binevski et al. 2019) to avoid degradation in vivo, achieve controlled release, and even reduce the immune response resulting from the payloads.

Compared with organic drug delivery systems, such as liposomes and synthetic copolymers, vaterite nanospheres are cost-efficient (Vikulina et al. 2020), safe (Trushina et al. 2022), and with an intrinsic degradation in the acidic tumor microenvironment (Som et al. 2016). Besides, they can release CO_2 bubbles in tumor tissues (pH 6.8–7.2) as a contrast agent for real-time ultrasound imaging (Min et al. 2015); and once endocytosed into lysosomes (pH 4.0–4.5), they also release CO_2 (Wang et al. 2018), potentially blasting lysosomes for the payload escape to the cytoplasm. Lysosomal escape is essential for antitumor drugs including doxorubicin (DOX), which then diffuses into the nuclei to disrupt DNA synthesis there (Agudelo et al. 2016).

However, the drawbacks of vaterite particles as drug carriers are obvious. Bare vaterite particles lack phase and colloidal stability; this stability guarantees prolonged blood circulation prior to accumulation in tumors. Passive accumulation is due to the presence of leaky vessels in tumors, with pores from 100 nm to 2 μm in diameter (Kalyane et al. 2019), highlighting the suitable particle sizes of nanomedicines (e.g., several hundred nanometers). Too small particles tend to be cleared by the reticuloendothelial system in the liver and the spleen. In some cases, active accumulation is achieved by grafting with specific ligands (e.g., folic acid (Shi et al. 2012)) that recognize tumor cells. This, however, requires reactive groups that are absent on bare vaterite particles.

Some bioactive molecules (Yang et al. 2016; Dong et al. 2016; Xu et al. 2022; Kim et al. 2013) and synthetic polymers (Popova et al. 2021; Min et al. 2015) have been used to template vaterite mineralization. Vaterite particles with nano range sizes, as well as long-term phase and colloidal stability (Popova et al. 2021; Xu et al. 2022; Kim et al. 2013), have been achieved in some formulations. To add reactivity, vaterite particles have been coated with specifically designed lipid layers with reactive groups to conjugate with targeting molecules (Dong et al. 2016; Xu et al. 2022; Kim et al. 2013), which complicates the preparation process and largely increases the material cost. Until now, a simple and

economical synthesis to achieve submicron size, long-term colloidal stability, as well as reactivity in one vaterite formulation remains a challenge.

As one of the most extensively studied polycationic materials, polyethylenimine (PEI) plays an important role in gene delivery therapy (Kircheis et al. 2001; Buscail et al. 2015; Pandey and Sawant 2016; Cao et al. 2021). Moreover, PEI contains CO_2-philic amino groups, making it an attractive CO_2 absorbent that has been extensively investigated for CO_2 capture (Shen et al. 2017). In this study, using the advantage that PEI absorbs CO_2, we used PEI-CO_2 adduct as a CO_2 source for $CaCO_3$ mineralization, leading to a mesoporous particulate form of $CaCO_3$ with a high surface area under mild conditions. The porous structure is perfect for the loading of both small and large biomolecules (Volodkin et al. 2004). The PEI as a template can maintain vaterite colloidal particles in an aqueous solution for over 8 months. Besides the high stability, the amino groups of PEI chains on vaterite particles provide reactive sites for further potential functionalization. Considering that a long circulation in the blood is necessary for tumor cellular internalization (Sun et al. 2014, 2017), poly(ethylene glycol) (PEG) was chosen to graft onto the vaterite nanoparticles through dynamic chemical bonds, making the particles "stealthy" in the blood (pH 7.4) but "activated" for cell internalization in acidic tumor tissues due to the departure of PEG chains (Chen et al. 2018). Doxorubicin (DOX) was selected as a model drug to be loaded into the vaterite $CaCO_3$ particles by the coprecipitation method. The strategy of tumor-triggered intracellular drug release is shown in Fig. 1, with folic acid (FA) as a tumor-targeting molecule (Shi et al. 2012).

Experimental section

Materials

Polyethylenimine (PEI, $M_n = 10$ k Da) was purchased from Gobekie New Materials Co., Ltd. (Shanghai, China). Calcium hydroxide (95%), 4-hydroxy benzaldehyde (98%), and *p*-toluenesulfonyl chloride (99%) were purchased from Chron Chemical Co., Ltd.
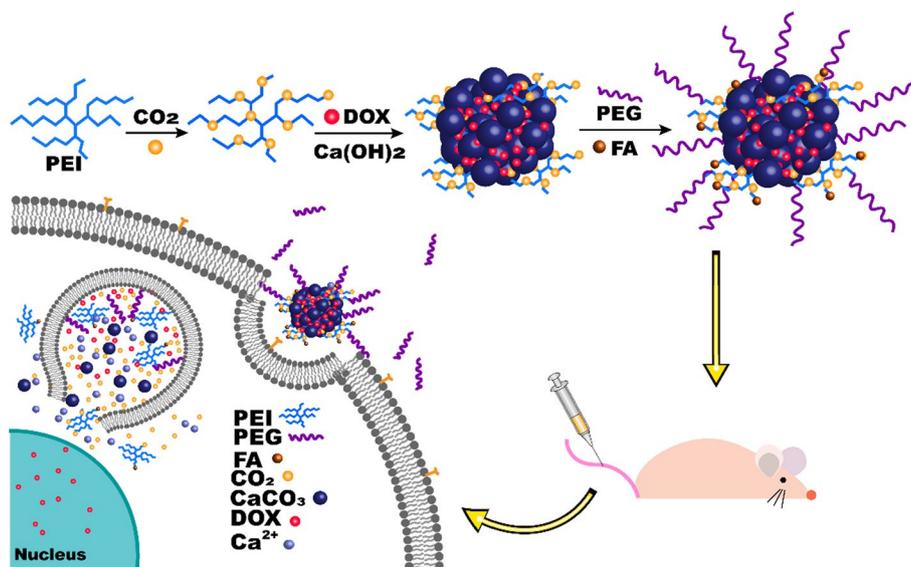
Fig. 1 Schematic design of tumor-triggered intracellular drug release of DOX/PEI-CO_2@$CaCO_3$-PEG-FA

(Chengdu, Sichuan, China). Fluorescein 5-isothiocyanate (FITC, 95%), doxorubicin hydrochloride (DOX, 98%), methoxy-polyethylene glycol (PEG, $M_n = 1,900$), and folic acid (FA, ≥ 97%) were purchased from Aladdin Biochemical Technology Co., Ltd. (Shanghai, China). Fluo-4 AM was purchased from Beyotime Biotechnology Co., Ltd. (Shanghai, China), and Lyso-Tracker Red was purchased from Solarbio Life Sciences Co., Ltd. (Beijing, China). The L929 and HeLa cells were donated by the West China School of Pharmacy, Sichuan University, China. The BALB/c-Nude mice (SPF) were purchased from Gempharmatech Biological Co., Ltd. (Jiangsu, China). Dulbecco's modified Eagle's medium (DMEM) was obtained from Thermo Fisher Scientific (China) Co., Ltd. (Shanghai, China). Fetal bovine serum (FBS), 2-[4-(2-Hydroxyethyl)piperazin-1-yl] ethanesulfonic acid (HEPES), Cell-Counting Kit-8 (CCK-8), and 4',6-diamidino-2-phenylindole (DAPI) were purchased from Biosharp Life Sciences (China) Co., Ltd. (Hefei, Anhui, China).

Synthesis of α-methoxy-ω-*p*-formylphenyl poly(ethylene glycol) (PEG-CHO)

The PEG-CHO was prepared as described elsewhere (Heathcote et al. 2007; Zhu et al. 2010). In brief, 20.0 g of PEG and 2.0 g of NaOH were added to 50 mL of tetrahydrofuran (THF), followed by stirring in an ice bath for 30 min. Afterward, 7.6 g of *p*-toluenesulfonyl chloride (TsCl) dissolved in 30 mL of THF was dropped into the PEG solution. After 4 h of reaction, 100 mL of ice water was added, and the mixture was extracted with 200 mL of CH_2Cl_2 three times. The organic phase was washed with deionized water and saturated NaCl solution. The washed organic layer was evaporated and concentrated, and 250 mL of absolute ether was poured to obtain a white precipitate. After filtration, the precipitate was vacuum dried at 50 °C for 1 d to obtain a white solid powder (PEG-OTs). Then, 15.0 g of the white powder, 19.3 g of anhydrous K_2CO_3, 2.6 g of *p*-hydroxybenzaldehyde, and 100 mL of anhydrous CH_3CN were added into a flask and refluxed for 48 h at 85 °C in an N_2 atmosphere. The reaction product was distilled under reduced pressure to remove the solvent, and 200 mL of deionized water was added to dissolve the crude product. The dissolved product was extracted with 50 mL CH_2Cl_2 three times and precipitated with 500 mL absolute ether to obtain a white solid PEG-CHO.

Synthesis of polyethylenimine-CO_2 adduct templated $CaCO_3$ nanoparticles

The CO_2 atmosphere was introduced into 80 mL of 0.1 g/mL PEI aqueous solution for 48 h to obtain the PEI-CO_2 adduct (Additional file 1: Figure S1), into which 800 mL of $Ca(OH)_2$ solution (saturated at 25 °C) was slowly dropped under vigorous stirring at 37 °C for 6 h to obtain a PEI@$CaCO_3$ white emulsion, which was equally divided into four parts. The first part was spiked with a solution of 4 g PEG-CHO in 20 mL deionized water. The second part was spiked with 0.4 g of FA, which had been dissolved in 20 mL deionized water and activated with 0.35 g of 1-(3-dimethylaminopropyl)-3-ethyl-carbodiimide hydrochloride (EDC) for 40 min. After adding the functioning molecules, the two parts were stirred at 37 °C for 24 h in darkness. The third part was allowed to react with 4 g of PEG-CHO and then with 0.35 g of FA, the same as those described for the first and second parts. The last part was kept without any treatment. The obtained PEI@$CaCO_3$-PEG, PEI@$CaCO_3$-FA, PEI@$CaCO_3$-PEG-FA, and PEI@$CaCO_3$ suspensions were dialyzed against water through a regenerated cellulose membrane (Biosharp,

Hefei, Anhui, China) with a molecular weight cutoff (MWCO) of 10,000 Da for 2 d, with refreshing water at every 8 h. The dialysis retentates were rotary evaporated at 45 ℃ for 3 h and freeze dried at 20–30 Pa for 1 d. The resultant powders were ground under a CO_2 purge gas and then saturated with CO_2 at 0.6 Mpa for 24 h in a steel container to obtain the final products, namely PEI-CO_2@$CaCO_3$-PEG, PEI-CO_2@$CaCO_3$-FA, PEI-CO_2@$CaCO_3$-PEG-FA, and PEI-CO_2@$CaCO_3$.

Synthesis of doxorubicin-loaded PEI-CO_2@$CaCO_3$ nanoparticles

Thirty mL of DOX aqueous solution (5 mg/mL) was added into 60 mL of PEI-CO_2 solution (containing 6 g PEI) under vigorous stirring. Into the mixture, 600 mL of $Ca(OH)_2$ solution (saturated at 25 °C) was slowly dropped in 50 min. When the solution had turned translucent, the reaction mixture was ultrasonicated for 1–2 min to guarantee homogenous mixing and, thereafter, the reaction went on until a purple emulsion was formed, which was equally divided into three parts. The first part was kept without treatment, the second part reacted with 0.4 g FA, and the third part was grafted with 4 g PEG-CHO and then with 0.4 g FA. The reaction process was the same as that described for the corresponding $CaCO_3$ particles without DOX (See the above section). Each of the three suspensions with DOX was concentrated to about 100 mL via rotary evaporation at 45 ℃ for 2 h. The concentrated specimens were placed into 50-mL ultrafiltration tubes (MWCO 30 k Da, Millipore, MA, USA) and centrifuged at 9500 rpm (i.e., 11,600 *g*) (TGL-20 M, Shanghai Lu Xiangyi Centrifuge Instrument Co., Ltd., Shanghai, China). The retentates were further treated with another three cycles of resuspension-centrifugation to remove water-soluble impurities. The obtained precipitates were freeze dried, ground, and saturated with CO_2, as described for the corresponding $CaCO_3$ particles without DOX (See the above section). The final products were designated by adding "DOX/" before the sample code of the corresponding blank $CaCO_3$ nanoparticles (e.g., DOX/PEI-CO_2@$CaCO_3$).

The as-synthesized DOX-loaded $CaCO_3$ nanoparticles were vacuum dried at 100 °C for 1 h to release CO_2 from the PEI-CO_2 adduct in the particles, leading to specimens designated as DOX/PEI@$CaCO_3$, DOX/PEI@$CaCO_3$-FA, and DOX/PEI@$CaCO_3$-PEG-FA.

Characterizations of nanoparticles

The morphology of nanoparticles was characterized by scanning electron microscopy (SEM, Quanta 250, FEI, USA) and transmission electron microscopy (TEM, JEM-1200, JEOL, Japan). The polymorph of different nanoparticles was recorded by X-ray diffractometry (XRD, Ultima IV, Rigaku, Japan). Thermogravimetric analysis (TGA) was performed on a TG209F1 thermogravimetric analyzer (Netzsch, Germany). The structure of PEIs in the nanoparticles was analyzed by nuclear magnetic resonance (NMR, AVIII HD-400 MHz, Bruker, Germany) and X-ray photoelectron spectroscopy (XPS, Thermo Kalpha, Thermofisher, USA). Nanoparticles were dissolved in trifluoroacetic acid and then added to D_2O, ready for NMR analysis. The zeta potential and particle size of all nanoparticles were measured by particle size potentiometry (Zetasizer Nano ZSP, Marvin, UK).

pH-dependent decomposition of blank and drug-loaded PEI-CO$_2$@CaCO$_3$ nanoparticles

In vitro Ca^{2+} release experiments for various nanoparticles were performed in phosphate buffer solution (PBS) at pH 7.4, 6.5, or 5.5. The nanoparticle solution (10 mL at 1 mg/mL) was sealed in a dialysis bag (MWCO: 5000 Da) and shaken in 400 mL PBS with a predesigned pH value at 37 ℃. The PBS (4 mL) was withdrawn at predetermined time intervals and replaced with an equal volume of fresh medium. Into the withdrawn PBS, we added 2 mL Arsenazo III solution (0.2 mM, in HEPES-buffered saline at pH 7.4, where [HEPES] = 20 mM and [NaCl] = 150 mM). The absorbance of the solution at 656 nm was then measured, and the concentration of Ca^{2+} ions was calculated based on the standard curve.

To observe CO$_2$ bubble formation, about 2 mg DOX/PEI-CO$_2$@CaCO$_3$-PEG-FA and DOX/PEI@CaCO$_3$-PEG-FA powder were dispersed in 5 mL PBS (pH 7.4 or 6.5), respectively. The CO$_2$ release was observed under an optical microscope (Olympus BX 43, Japan) after 2 h.

In vitro DOX release profiles of drug-loaded nanoparticles were examined in PBS at pH 7.4, 6.5, or 5.5. Both the nanoparticle specimens with 600 μg DOX equivalent and free DOX of 600 μg were added to 10 mL PBS and transferred to a dialysis membrane bag (MWCO: 5000 Da). The latter served as a control. The release experiment was initiated by placing the dialysis bag in 100 mL of PBS at different pH values. The releasing medium was shaken at 37 ℃, and at predetermined time intervals, samples (5 mL) were withdrawn and replaced with an equal volume of fresh PBS. The concentration of released DOX in the samples was determined by the measurement of fluorescence emission intensity at 588 nm (excitation at 480 nm), based on the standard curve obtained using DOX. Note that the DOX loadings in CaCO$_3$ particles were determined in the same way after the dissolution of the CaCO$_3$ powders in HCl solution, and calculated as Drug loading (%) = Mass of encapsulated DOX/(Mass of carriers + Mass of encapsulated DOX) × 100%.

Cytotoxicity of blank and drug-loaded PEI-CO$_2$@CaCO$_3$ nanoparticles

For the cell viability measurements, HeLa cells in DMEM suspension were seeded in 96-well plates (5×10^3 cells per well) and allowed to grow overnight. Subsequently, the medium was discarded, and all wells were washed twice with fresh PBS. Then, 200 μL of serum-free DMEM containing DOX or CaCO$_3$ nanoparticles at predesigned concentrations was added to each well. After 24 h and 48 h of co-incubation, cell viability was assessed with a CCK-8 assay. Briefly, the medium was replaced with an equal volume of fresh medium containing CCK-8 and incubated for 30 min at 37 ℃. The viable cell number was proportional to the absorbance of each well at 450 nm, recorded by a microplate reader (Biorad Elizer, PA). The data were normalized to the cell viability of the control group that grew in the same DMEM without DOX or nanoparticles.

Endocytosis of blank PEI-CO$_2$@CaCO$_3$ nanoparticles

To monitor the cellular uptake of the blank PEI-CO$_2$@CaCO$_3$ nanoparticles, the nanoparticles were fluorescently labeled with FITC. In brief, 500 mg nanoparticle powder with 90 mg FITC dispersed in deionized water was stirred in the dark for 2 d and then

freeze dried after dialysis (MWCO: 10 k Da) for another 2 d. The labeled nanopowder was redispersed in serum-free DMEM at a concentration of 50 μg/mL. Subsequently, HeLa or L929 cells suspended in 2 mL of DMEM supplemented with 10% FBS and 1% antibiotics were seeded onto round coverslips in individual wells of a 6-well plate (1×10^6 cells/mL, 2 mL/well). After incubation to 80% confluence (5% CO_2, 75% humidity, 37 °C), the medium was aspirated and replaced with 2 mL of the medium containing FITC-labeled nanoparticles. The cells were incubated for 4, 8, and 12 h, washed with PBS three times and fixed with 4% paraformaldehyde for 15 min. The fixed cells were stained with 10% DAPI for 5 min, washed with PBS again, sealed with antifading mounting medium (S2100, Solarbio, Beijing, China), and observed under a Leica TCS SP5II confocal laser scanning microscope (CLSM, Leica, Mannheim, Germany). In addition, the cells incubated with different nanoparticles for 12 h were digested with 0.25% trypsin, centrifuged and resuspended in PBS, and passed through a 60-mesh cell strainer to obtain a single-cell suspension; the uptake of nanoparticles was quantitatively analyzed by flow cytometry (FCM, BD LSRFortessa, USA).

To reveal the location of nanoparticles in cells, HeLa or L929 cells were seeded onto round coverslips in a six-well plate at a density of 1×10^5 cells per well. After cell adherence, the original FBS-containing DMEM medium was replaced with an equal volume of suspension containing FTIC-labeled nanoparticles (10 μg/mL). After 4 h of incubation, cells were washed three times with PBS, followed by the addition of Lyso-Tracker Red (75 nM) medium to incubate for another 30 min. Then, the cells were washed with PBS again, fixed with paraformaldehyde, and finally stained with DAPI. Samples were subjected to CLSM observation. The location of Ca^{2+} ions in cells was observed in the same way, except that the nanoparticles were not labeled with FITC, and Ca^{2+} ions in the cells were labeled instead. In detail, the Ca^{2+} ions were labeled with Fluo-4 AM (5 μM) in the DMEM for 30 min after 4 h of incubation in the original medium. The cells were washed with PBS and further labeled with Lyso-Tracker Red to indicate lysosomes.

To observe the dynamic release of Ca^{2+} ions in cells, HeLa cells were incubated in the original medium for 3 h, and Ca^{2+} ions were labeled with Fluo-4 AM, as described previously. Live cell imaging was recorded every 5 min within 30 min under a CLSM.

Location of DOX/PEI-CO$_2$@CaCO$_3$-PEG-FA nanoparticles in cells by TEM

The HeLa cells were seeded into a 100-mm petri dish at 3×10^7 cells/dish and incubated overnight in 15 mL of FBS-containing DMEM medium. The original medium was replaced with an FBS-free DMEM medium containing DOX/PEI-CO_2@$CaCO_3$-PEG-FA at 50 μg/mL. After 4 h of incubation, the cells were rinsed with PBS three times, scraped from the petri dish with a cell scraper, and placed in a centrifuge tube to obtain a mung bean-sized cell spheroid via centrifugation. The cell spheroid was fixed in glutaraldehyde solution at 4 °C overnight, embedded in paraffin, and sliced for observation under a biological transmission electron microscope (FEI-Tecnai SPIRIT, USA).

Intracellular drug release of various drug-loaded PEI-CO$_2$@CaCO$_3$ nanoparticles

The HeLa cells were seeded onto round coverslips in a six-well plate at 1×10^5 cells per well and incubated overnight. The original medium was replaced with serum-free DMEM containing free DOX or DOX-loaded nanoparticles at 1 μg/mL DOX equivalent.

After a predetermined incubation period, cells were washed several times with PBS, fixed with paraformaldehyde, and stained with DAPI, followed by CLSM observation.

In vivo biodistribution assay of blank PEI-CO$_2$@CaCO$_3$ nanoparticles

The BLBC/c-Nude mice were used for animal experiments. All animal experiments were performed in compliance with the guidelines for the care and use of laboratory animals. The tumor model was established subcutaneously by inoculating 1×10^8 HeLa cells into the right back of a mouse. To avoid fluorescence from DOX, blank nanoparticles labeled with FITC were used to analyze the in vivo biodistribution. The labeled nanoparticles (5 µg in 100 µL PBS) were administrated via tail vein injection into tumor-bearing nude mice. At 24 h post-injection, the fluorescent images were recorded using an in vivo imaging system (IVIS Spectrum, Perkin Elmer, USA). After live imaging, mice were killed, and the main organs and tumor tissues were excised for ex vivo imaging using the same imaging system.

In vivo antitumor effect

When the xenograft tumor had reached around 50 mm^3, mice were randomly divided into five groups ($n=7$) and intravenously injected with 200 µL saline containing free DOX or DOX-loaded CaCO$_3$ particles at 1 mg/kg DOX equivalent. The group injected with 200 µL saline served as a control. The day of administration was defined as Day 0. The administration was performed every 2 d over a 14-d therapeutic period. Tumor volume and body weights were measured. At Day 14, three mice in each group were randomly selected and euthanized. The tumors were collected, weighed, washed with saline thrice, and fixed in 10% formalin. The fixed tumors were embedded in paraffin to prepare sections for hematoxylin–eosin (HE) staining. Tissue images were recorded at $200 \times$ magnification under an optical microscope (Pannoramic 250, 3DHISTECH Ltd., Budapest, Hungary). The survival rate was calculated for up to 30 d.

Statistical analysis

Quantitative data were presented as mean ± standard deviation (S.D.) from triplicate experiments ($n=3$) performed in a parallel manner unless otherwise stated. Statistical significance was tested by two-tailed Student's t-test or one-way ANOVA, where $P < 0.05$ (*) and $P < 0.01$ (**) were considered statistically significant.

Results

Chemical structures and composition of as-synthesized CaCO$_3$ particles

The presence of aldehyde C=O stretching at 1690 cm^{-1} and benzene ring breathing stretching at 1600 cm^{-1} indicated the successful synthesis of PEG-CHO (Additional file 1: Figure S2). Accordingly, the signals of aldehyde proton at 9.98 ppm and benzene ring protons at 7.77 and 7.33 ppm appeared in the ^{1}H NMR spectrum of PEG-CHO (Additional file 1: Figure S2).

The organic chemicals in the as-synthesized CaCO$_3$ particles were characterized by ^{1}H-NMR in D$_2$O after the dissolution of the CaCO$_3$ particles with trifluoroacetic acid. As shown in Fig. 2, the hydrolysis of the Schiff base group in an acidic environment would restore the aldehyde group and, therefore, the proton signal from aldehyde could
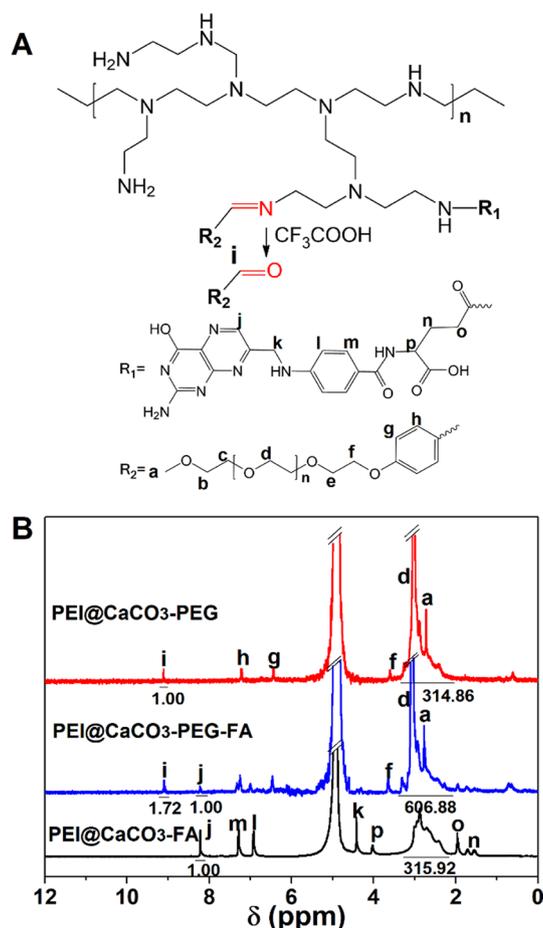
Fig. 2 ^{1}H NMR spectra of three CaCO$_3$ particles dissolved in trifluoroacetic acid and D$_2$O. **A** Chemical structure of modified PEIs, where the PEG side chains had restored the aldehyde terminal groups (see red groups). **B** Assignment of the NMR spectra. The presence of Ca^{2+} had altered the chemical shift. For instance, the PEG proton signal usually appears at 3.5 ppm, but here, it appears at 3.0 ppm

be found at 9.13 ppm in the PEI@CaCO$_3$-PEG specimen, with benzene ring protons at 6.43 and 7.22 ppm. The PEG protons (–CH$_2$CH$_2$O–, peak d) at 3.01 ppm partially overlapped with PEI ethylene signals, ranging from 2.25 to 3.36 ppm. After grafting with folic acid (FA), additional signals associated with FA appeared in the spectra of the PEI@ CaCO$_3$-PEG-FA specimen, such as pyrimidine ring proton at 8.23 ppm (peak j). Reasonably, the PEI@CaCO$_3$-FA specimen displayed proton signals from both PEI and FA.

All FTIR spectra (Fig. 3A and B) showed absorptions at 1485 and 875 cm^{-1} due to the unique symmetrical stretching and bending vibration of CO$_3^{2-}$ in CaCO$_3$. In addition, the weak N–H and C–H vibration peaks due to the presence of PEI backbones could be seen at 3300 and 2887 cm^{-1}, respectively. The specimens containing PEG chains displayed absorption of C–O–C stretching at 1100 cm^{-1}. After being loaded with DOX, the specimens showed a much stronger absorption at 3300 cm^{-1}, resulting from hydroxyl and amine groups in DOX, as well as an additional absorption at 1630 cm^{-1} from the carbonyl groups in DOX. Moreover, the survey scan of the XPS analysis (Additional file 1: Figure S3) showed the presence of C, N, O, and Ca in PEI-CO$_2$@CaCO$_3$-PEG-FA. The high resolution of the C$_{1S}$ scan displayed a major

Luo *et al. Cancer Nanotechnology* (2023) 14:7

Page 10 of 21
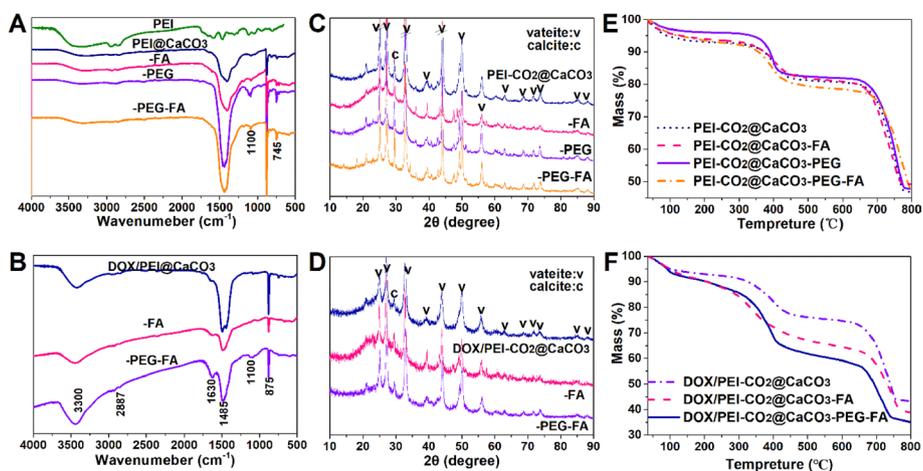
Fig. 3 Structural analyses of bare (top) and drug-loaded (bottom) $CaCO_3$ nanoparticles

Table 1 Composition of as-synthesized $CaCO_3$ nanoparticles

Sample	Weight loss by TG (wt%)			Residue[a] (wt%)	$CaCO_3$[b] (wt%)	DOX loading (wt%)
	CO_2 (PEI-CO_2)	Organic substance	CO_2 ($CaCO_3$)			
PEI-CO_2@$CaCO_3$	6.42	12.72	33.94	46.92	77.19	
-PEG	3.00	14.95	34.18	47.87	77.73	
-FA	5.65	12.99	32.11	49.25	73.03	
-PEG-FA[a]	3.92	17.64	30.53	47.93	69.39	
Durg-loaded						
PEI-CO_2@$CaCO_3$	5.78	18.73	32.16	43.33	73.14	5.91
-FA	6.98	27.14	26.62	39.00	60.54	6.55
-PEG-FA	7.82	31.79	25.36	35.03	57.68	5.79

[a] The residue was obtained at the final temperature (bare particles: 795 °C; drug-loaded particles: 765 °C)

[b] The $CaCO_3$ content was calculated from the third weight loss (i.e., CO_2 content from $CaCO_3$)

$C=N(C-O)$ peak at 286.5 eV (from FA), being companied by a $C-C$ peak at 284.5 eV (from PEI and PEG) and a $C=O$ peak at 288 eV (from FA). The high resolution of the N_{1S} scan displayed a major $C-N$ peak at 399 eV (from PEI and FA) and a minor $C=N$ peak at 401 eV (from both FA and the Schiff base linkage between PEI backbone and PEG side chains).

The XRD patterns (Fig. 3C, D) revealed that all $CaCO_3$ nanoparticles had a vaterite crystal form, with minor calcite crystals. All specimens showed a typical broad peak at 2θ of 25° due to the presence of amorphous PEI. Loading with DOX did not change the crystal form of $CaCO_3$.

The TG curves before and after drug loading, as shown in Fig. 3E, F, displayed three weight loss processes, centered at about 60 °C, 390 °C, and 740 °C, which can be assigned to the CO_2 release from PEI-CO_2 adduct, thermal decomposition of the organic substances, and the decomposition of $CaCO_3$, respectively. The detailed composition based on TG analysis can be found in Table 1. Grafting with PEG and FA could reduce the $CaCO_3$ content in the nanoparticles, and the loading of DOX (5.79–6.55%) could further lower it down to about 58%.

Morphology and particle size of as-synthesized CaCO₃ particles

All specimens displayed spherical morphology, without obvious changes before and after being loaded with DOX (Fig. 4 and Additional file 1: Figure S4). A thin, gray layer was found around individual nanoparticles under TEM, which was due to the presence of PEI polymers (Fig. 4C). The average particle size was slightly enhanced after loading with DOX (Fig. 4E), whereas the zeta potential was decreased (Fig. 4F) a little. All specimens showed positive zeta potentials, consistent with the cationic PEI nature. Specimens with PEG chains demonstrated lower zeta potentials than their counterparts without PEG chains, suggesting a charge shielding effect due to the neutral PEG chains (Additional file 1: Figure S4).

In vitro particle decomposition and drug release of as-synthesized CaCO₃ particles

The Ca^{2+} release behavior of drug-loaded particles at different pH values is shown in Fig. 5A. The particles were stable at pH 7.4, and Ca^{2+} release was faster at lower pH values. The CO_2 saturation of PEI could accelerate Ca^{2+} release. A reduction in Ca^{2+} release rate was observed when the PEI-CO_2 adduct in CaCO₃ was heated to restore the PEI polyamine structure (Fig. 5B). The same trends of DOX release could be observed for DOX-loaded specimens (Fig. 5C, D), suggesting that DOX release was due to the acidic dissolution of CaCO₃ nanoparticles. As expected, free DOX diffused very quickly through the dialysis membrane (indicated by an arrowed line, Fig. 5D). In addition, the Ca^{2+} release behavior of blank CaCO₃ particles was almost the same as that of drug-loaded counterparts (Additional file 1: Figure S5), indicating that drug loading could not affect the dissolution of CaCO₃ particles. Besides the release of Ca^{2+}, the formation of CO_2 bubbles could be observed as another indicator of CaCO₃ dissolution (Additional file 1: Figure S6).

Cytotoxicity, endocytosis, and drug release into cells

The blank CaCO₃ nanoparticles showed toxicity to both HeLa and L929 cells, albeit only at high concentrations (e.g., 100 µg/mL) (Fig. 6A, B). At the same dosage, HeLa cells were less viable that L929 cells, possibly due to the strong metabolism of HeLa
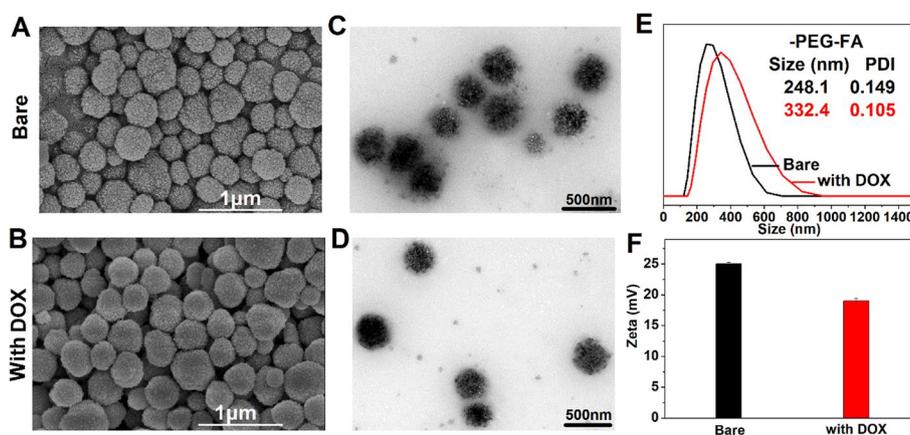
Fig. 4 Morphological observation of PEI-CO_2@CaCO₃-PEG-FA nanoparticles **A**–**D** and the dynamic light scattering results **E**, **F**
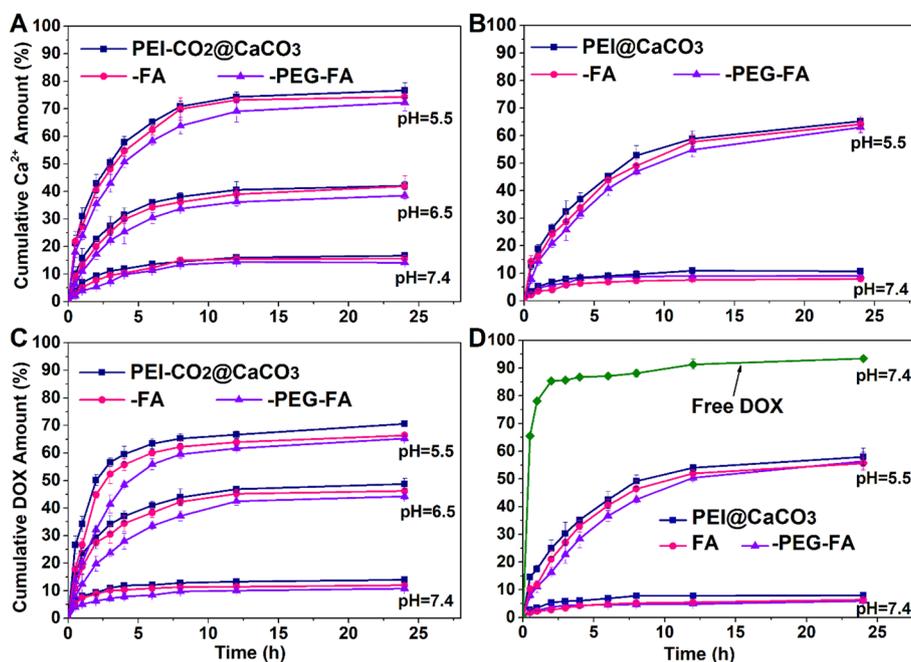
Fig. 5 In vitro Ca^{2+} and DOX release behavior of drug-loaded $CaCO_3$ nanoparticles. The Ca^{2+} and DOX released more swiftly in the particles with $PEI-CO_2$ **A**, **C** than in those with PEI **B**, **D**. For free DOX, over 80% of DOX was released through the dialysis membrane in 2 h **D**
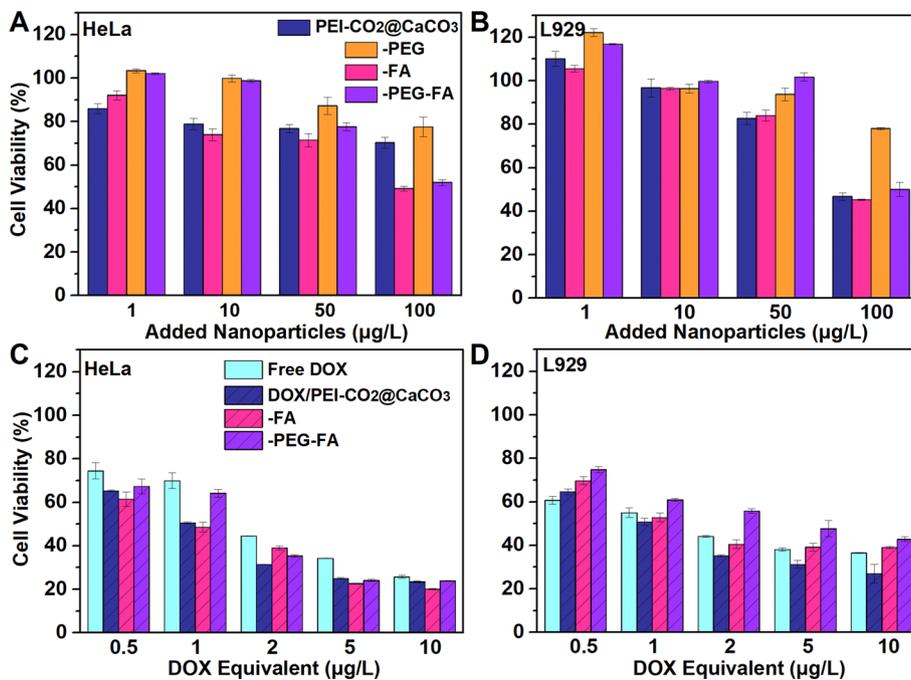
Fig. 6 Test of cytotoxicity of as-synthesized $CaCO_3$ nanoparticles. Cell viability is normalized to that of the control group in the DMEM medium

cells and the strong acidity of the cell environment, which caused a fast decomposition of the $CaCO_3$ nanoparticles. Among the blank $CaCO_3$ specimens, PEI-CO_2@$CaCO_3$-PEG demonstrated the lowest toxicity, due to the presence of a biocompatible PEG surface layer. After being loaded with DOX, obvious cytotoxicity was observed at very low dosages (Fig. 6C, D) for all specimens.

Various $CaCO_3$ nanoparticles labeled with FITC were incubated with HeLa and L929 cells and observed under a CLSM. As shown in (Additional file 1: Figure S7), both cells could phagocytose the $CaCO_3$ nanoparticles in 4 h, with HeLa cells containing more particles. The corresponding flow cytometry data (Fig. 7A) further revealed that HaLa cells phagocytosed more nanoparticles grafted with FA, whereas
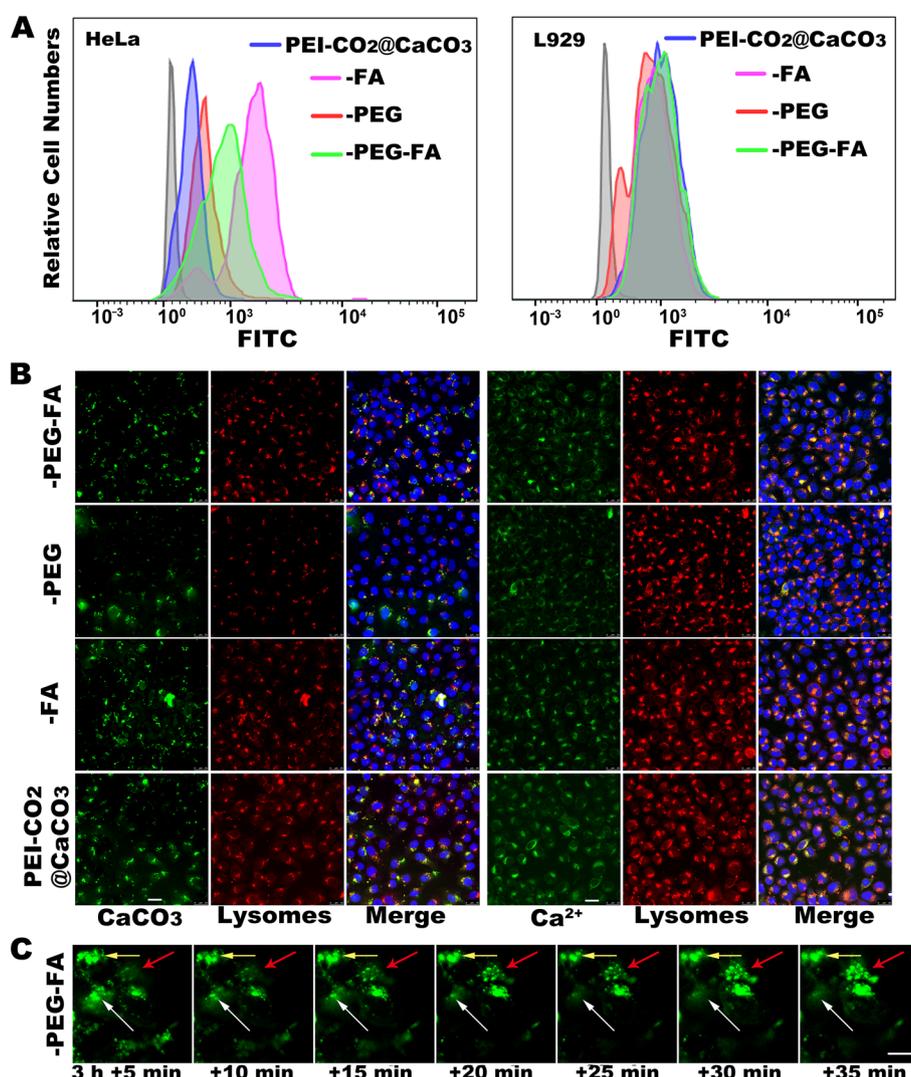

Fig. 7 Endocytosis of various $CaCO_3$ nanoparticles. **A** Flow cytometry showed HeLa cells endocytosed more FA-grafted particles. **B** Fluorescence staining revealed both particles and the released Ca^{2+} ions located in lysosomes. Scale bars: 25 μm. **C** Dynamic change of local Ca^{2+} fluorescent intensity after incubation with PEI-CO_2@$CaCO_3$-PEG-FA particles. Scale bar: 10 μm

L929 cells responded equally to all types of $CaCO_3$ specimens. This suggests that the expression of FA receptors on HeLa cells might facilitate particle endocytosis.

As shown in Fig. 7B, the fluorescence staining technique revealed that both the endocytosed $CaCO_3$ nanoparticles and the released Ca^{2+} ions were located in the lysosomes of HeLa cells. The same location could be found for L929 cells (Additional file 1: Figure S8). The internalized $CaCO_3$ nanoparticles entered lysosomes where the acidic environment would decompose $CaCO_3$ nanoparticles, releasing both Ca^{2+} and CO_2 in situ. To deeply explore the release behavior of $CaCO_3$ nanoparticles in cells, we observed the dynamic changes in local fluorescence intensity of Ca^{2+} ions from endocytosed PEI-CO_2@$CaCO_3$-PEG-FA particles. Within a period of 30 min (Fig. 7C), we observed a gradual increase (red arrows) or decrease (white arrows) of local Ca^{2+} fluorescence intensity, as well as the maintenance of the intensity (yellow arrows), corresponding to the dissolution of $CaCO_3$, Ca^{2+} ion escape from lysosomes, and the balance between the dissolution and the escape, respectively.

The TEM could directly reveal the morphological changes in lysosomes due to encapsulation of the as-synthesized $CaCO_3$ nanoparticles (Fig. 8). Besides vesicle-like normal lysosomes (L, Fig. 8), the black spheres (C, Fig. 8) in the view field indicated those lysosomes encapsulated with the $CaCO_3$ nanoparticles. A bursting lysosome was attached to a small bubble surrounded by a black thick wall (B1, left, Fig. 8) or composed of several bubbles with thick walls (B1, right, Fig. 8). Some burst lysosomes (B2, left and right, Fig. 8) displayed irregular main bodies with gray debris scattered far away. Within some debris, empty bubbles surrounded by thick walls could be seen as well. The black or gray regions were due to the presence of a $CaCO_3$ phase, and the bubble-like structure was the result of the formation of CO_2 bubbles that pushed away the surrounding $CaCO_3$ phase. The TEM images clearly proved the burst of lysosomes due to the dissolution of the encapsulated $CaCO_3$, which released CO_2 bubbles to blow and break the lysosomes.

The delivery of DOX into cells was associated with the endocytosis and dissolution of the $CaCO_3$ carriers (Fig. 9). Free DOX entered the nuclei in only 2 h, almost without DOX in the cytoplasm. This is because that DOX can easily bind to nuclear DNA (Agudelo et al. 2016), and free DOX cannot stay in the cytoplasm in large amounts (left, Fig. 9). However, the DOX-loaded $CaCO_3$ specimens delivered DOX (via lysosomes) into the cytoplasm and then into the nuclei (via lysosomal escape). This could be clearly seen in the "PEI@" group (middle, Fig. 9), where the PEI-CO_2 adducts in the $CaCO_3$ particles
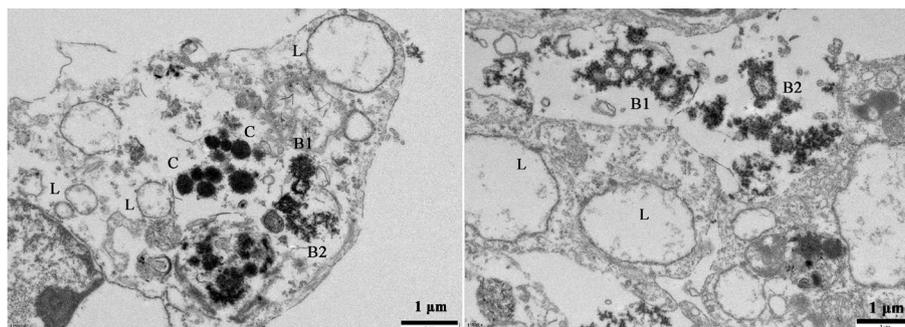
Fig. 8 PEI-CO_2@$CaCO_3$-PEG-FA particles were entrapped in lysosomes imaged by TEM. L: normal lysosomes; C: particles in lysosomes; B1: bursting lysosomes; B2: burst lysosomes

Luo *et al. Cancer Nanotechnology*   (2023) 14:7

Page 15 of 21
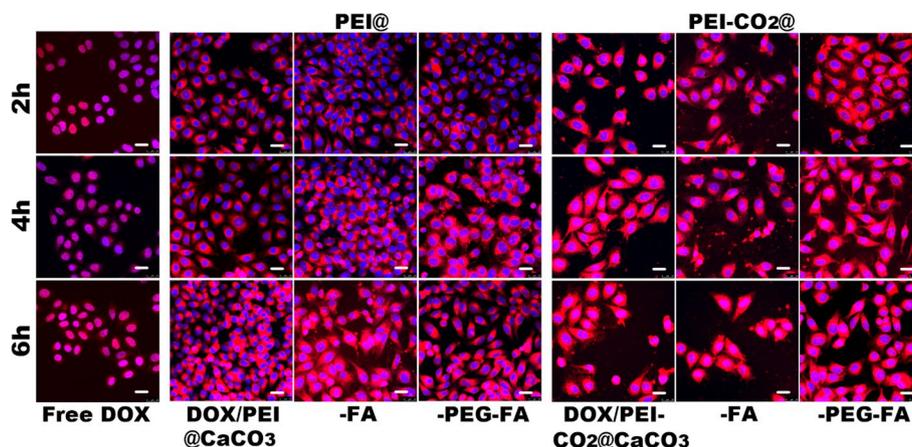
Fig. 9 Particles were incubated with HeLa cells, and the encapsulated DOX was released into the cells. The particles with PEI-CO_2 released DOX more rapidly (right group) than did the particles with PEI (middle group). Red: DOX; Blue: nuclei. Scale bars: 25 μm

had been transformed into the corresponding PEIs. For this group, DOX began to appear in the nuclei at 4 h and further accumulated there at 6 h. The particle type affected the DOX delivery considerably. Those specimens containing FA demonstrated more DOX in the nuclei at the same timepoint. For the "PEI-CO_2@" group (right, Fig. 9), where the PEI-CO_2 remained in the particles, DOX spread in the cytoplasm and reached the nuclei in 2 h. Thereafter, DOX accumulated in the nuclei as well. No obvious difference could be observed across the specimens in this group. The relatively fast decomposition of the PEI-CO_2@$CaCO_3$ particles in the acidic environment (Fig. 5) was responsible for the fast DOX delivery into nuclei, masking the influence of the particle type.

In vivo biodistribution and antitumor effects

The results of the in vivo distribution study (Fig. 10) showed that $CaCO_3$ nanoparticles were mainly concentrated in the liver and tumor in the HeLa-xenografted mice. The particle size was in the range of 200–300 nm, and the liver was the main metabolic organ; thereby, $CaCO_3$ nanoparticles accumulated in the liver. Besides the liver, nanoparticles could accumulate in the tumor via the passive enhanced permeability and retention (EPR) effect (Kalyane et al. 2019) or via FA-mediated targeting of tumor cells. Both could contribute to tumor accumulation in PEI-CO_2@$CaCO_3$-FA and PEI-CO_2@$CaCO_3$-PEG-FA specimens, whereas only the EPR effect played a role in the PEI-CO_2@$CaCO_3$ specimen, leading to lower tumor accumulation in the latter (Fig. 10C). The specimen containing PEG accumulated less in the liver than did the other two $CaCO_3$ specimens; PEG grafting reduced toxicity to the liver.

The DOX-loaded nanoparticles showed an antitumor effect (Fig. 11) in vivo. Among the saline- and nanoparticle-treated groups, tumor growth was significantly inhibited in the DOX/PEI-CO_2@$CaCO_3$-FA and DOX/PEI-CO_2@$CaCO_3$-PEG-FA groups, with a final tumor volume of 138 ± 82 mm^3 and 124 ± 67 mm^3, respectively, corresponding to a tumor inhibition rate of 79.6% and 81.7% with respect to the tumor volume (678 ± 107 mm^3) of the saline group. The inhibition rate was 47.2% and 26.8% for the DOX/PEI-CO_2@$CaCO_3$ and the free DOX group, respectively (Fig. 11A). The highest
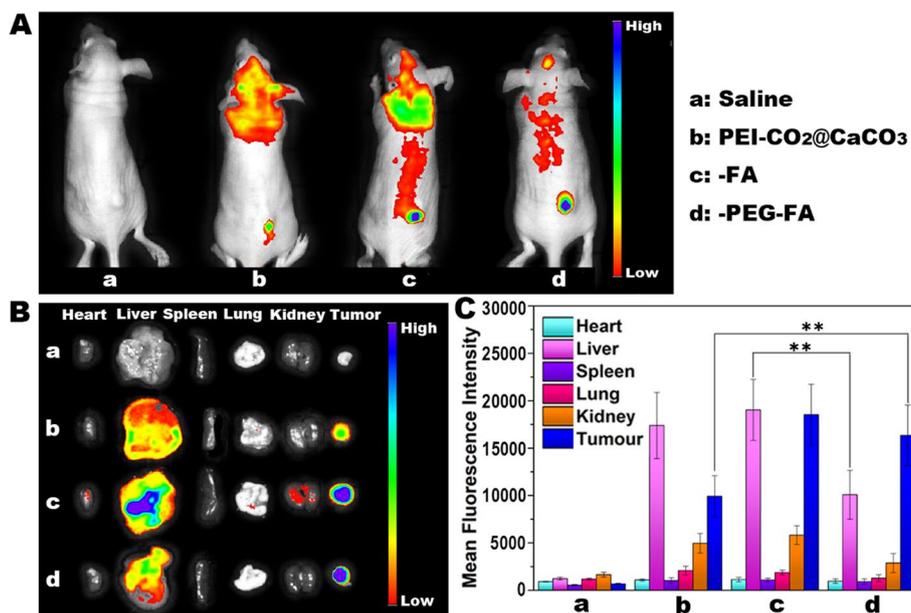
Fig. 10 Blank particles (without DOX) biodistribution in vivo
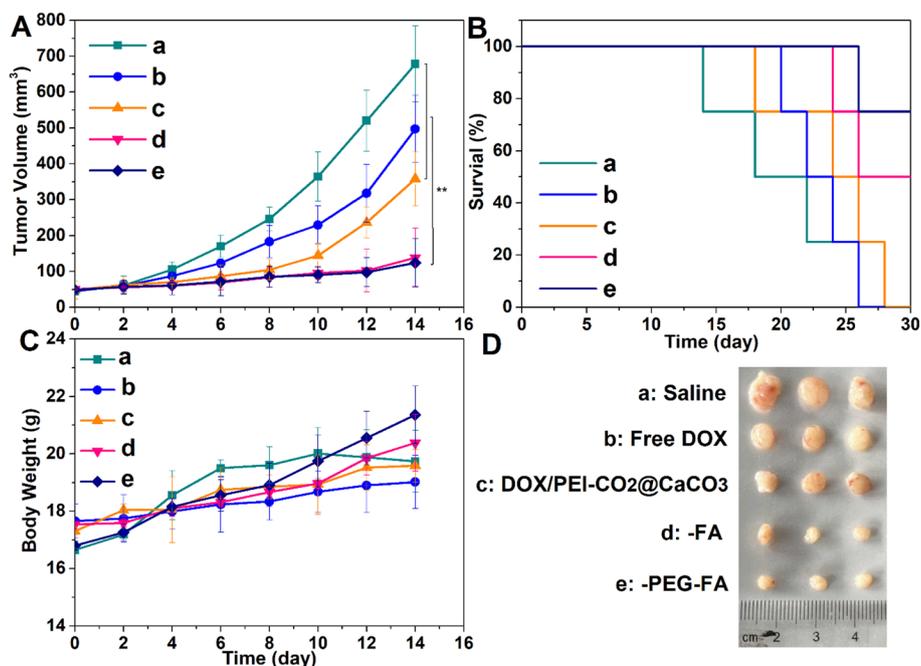
Fig. 11 Antitumor effects of various DOX-loaded CaCO$_3$ particles. The saline and free DOX served as controls

survival rate (Fig. 11B) and the largest gain of body weight (Fig. 11C) both proved that DOX/PEI-CO$_2$@CaCO$_3$-PEG-FA possessed the best antitumor effect. Direct observation of the tumor size clearly displayed the different antitumor effects across the investigated groups (Fig. 11D).

The tumor was sectioned and observed histologically (Additional file 1: Figure S9). The specimens treated with DOX/PEI-CO$_2$@CaCO$_3$-FA and DOX/PEI-CO$_2$@CaCO$_3$-PEG-FA had the largest necrosis areas, with a significantly reduced density of cell nuclei. At the final stage of the treatment, the main organs from each experimental group were taken for histological observation (Additional file 1: Figure S10). Only the free DOX group had a certain organic toxicity, whereas the other groups showed no abnormalities, indicating that the as-synthesized CaCO$_3$ nanoparticles effectively reduced the toxicity of free DOX.

Discussion

The unique porous structure of the vaterite polymorph of calcium carbonate makes it a good carrier to deliver drugs (Zhao et al. 2015; Min et al. 2015; Dong et al. 2016; Dizaj et al. 2019) and even vaccines (Wang et al. 2018) for cancer therapy. Previous investigations adopted various polymers (Som et al. 2016; Min et al. 2015) and biomolecules (e.g., ovalbumin (Wang et al. 2018), hesperidin (Yang et al. 2016), and capsaicin (Xu et al. 2022)) to stabilize the metastable vaterite particles. These stabilizers usually possess carboxylate anions or chelating groups that bind to Ca^{2+} cations during CaCO$_3$ formation. The obtained particles often maintain the vaterite polymorph for several days (Volodkin et al. 2004; Trushina et al. 2014; Boyjoo et al. 2014), beyond which it transforms into a thermodynamically stable and nonporous calcite phase. We used PEI-CO$_2$ adduct to template CaCO$_3$ formation. The PEI-CO$_2$ as the CO$_2$ source restricted the nucleation and growth of CaCO$_3$ crystals within the branched PEI backbones. The calcium source was a saturated Ca(OH)$_2$ solution. In this context, no salt byproduct was formed, simplifying the purification process. Moreover, PEI-CO$_2$ released CO$_2$ to form CaCO$_3$, leaving the PEI chains being tightly entangled with the primary CaCO$_3$ crystals. The entangled PEI chains could stabilize the obtained vaterite phase as colloidal particles in water for over 8 months (Additional file 1: Figure S11). Such long-term stability has not been observed in previously synthesized vaterite crystals. For example, high molecular PEIs have been observed to induce vaterite CaCO$_3$ formation at air–water interface (Park et al. 2004), using Ca(HCO$_3$)$_2$ as the raw material. The vaterite phase remained for 3 d in water.

As most nanomedicines for cancer therapy are administered via vein injection, colloidal stability in an aqueous environment is a prerequisite for blood circulation prior to accumulation in the tumor. For CaCO$_3$ drug carriers, the vaterite phase should be kept until delivery of the payload into tumor cells. Therefore, both colloid and phase stability of a period of at least several days (e.g., 2 d) should be required for a vaterite drug delivery system. However, for a real nanomedicine used clinically, such stability should be months to years, considering the time for manufacture, transport, and storage. Our observation of stability for 8 months is highly valuable as long-term stability data for vaterite drug carriers are lacking.

The reactivity of the amino groups from the PEI chains on and in the CaCO$_3$ nanoparticles facilitates the further functionalization of the nanoparticles. As shown in this study, PEG could be grafted to extend blood circulation (Cao et al. 2021) and to reduce the toxicity of encapsulated DOX to remote organs (e.g., liver) (Fig. 10C). Once reaching the tumor tissues, the PEI chains would be detached from the nanoparticles due to

the acidic breakdown of the Schiff base linkages. The cationic PEI chains on the nanoparticles would bind to the negatively charged cell membrane, facilitating endocytosis. In addition, FA could be also grafted to generate tumor targeting. It should be noted that PEG grafting and FA targeting have been widely used to enhance antitumor effects for decades (Greenwald 2001; Wang and Low 1998). The preferential biodistribution in mice tumor tissues (Fig. 10C) could account for the strong tumor inhibition of the drug-loaded vaterite nanoparticles that were grafted with FA (Fig. 11A), despite the fact that they possessed similar in vitro cytotoxicity as free DOX (Fig. 6C, D).

Previous investigations have shown several advantages of $CaCO_3$ in vaterite form as an antitumor drug carrier. First, it can dissolute in the acidic environment of tumor tissues (pH 6.8–7.2) to release CO_2, allowing for ultrasound imaging of cancers during chemotherapy via drug delivery (Min et al. 2015). Second, it can further dissolute in lysosomes (pH 4.0–4.5) after internalization to generate CO_2 bubbles to disrupt lysosomes, releasing the payload (Wang et al. 2018) to target subcellular counterparts. Compared with polymeric nanocarriers, $CaCO_3$ can easily be synthesized and is more economical but lacks in reactivity for further functionalization. Our formulation of $CaCO_3$ drug carriers keeps the intrinsic advantages of the vaterite polymorph and further provides reactivity due to the polyamine structure of the PEI stabilizer. Moreover, the PEI chains on and in the nanoparticles can absorb CO_2, forming the zwitterionic PEI-CO_2 adduct in situ. This adduct can release CO_2 in acidic environments, which can react with $CaCO_3$ to form water-soluble calcium bicarbonate ($Ca(HCO_3)_2$) (Park et al. 2004), accelerating the dissolution of $CaCO_3$. Therefore, PEI-CO_2-containing $CaCO_3$ particles released Ca^{2+} and DOX more swiftly than did the PEI-containing analogs (Fig. 5). Accordingly, faster delivery of DOX into the nuclei in the former was observed (Fig. 9). The additional CO_2 from the PEI-CO_2 templates would enhance the pressure of lysosomes, making them more easily disrupted and further accelerating DOX escape from lysosomes (Fig. 8). The PEI itself could act as a proton sponge, with the protonation in lysosomes causing osmotic swelling, which should also have contributed to the lysosomal rupture (Kircheis et al. 2001). The rapid delivery of DOX into nuclei must have contributed to the efficient therapy of the HeLa tumor in mice (Fig. 11).

The simple synthesis, long-term stability of the colloidal vaterite phase, ease of functionalization, and high CO_2 content of PEI-CO_2-templated $CaCO_3$ nanoparticles could provide a new platform for the delivery of therapeutic agents into cells, beyond the antitumor drugs shown in this study.

Conclusions

Here, we report a simple preparation of $CaCO_3$ nanoparticles using PEI-CO_2 and $Ca(OH)_2$ as the CO_2 and calcium sources, respectively. The PEI chains could template the formation of the vaterite polymorph of $CaCO_3$, stabilize the hydrocolloidal vaterite particles, and provide reactive amino groups for further potential functionalization. Both PEG and FA were grafted onto the $CaCO_3$ nanoparticles via acid-cleavable Schiff base linkage and relatively stable amide linkage, respectively. The PEI chains in the nanoparticles could further absorb CO_2 to restore the PEI-CO_2 adduct. The functionalized porous vaterite particles could

Luo *et al. Cancer Nanotechnology*   (2023) 14:7

Page 19 of 21

deliver DOX into HeLa cells via lysosomes. During the endocytosis process, the PEI-CO_2 adduct could release extra CO_2 to accelerate the $CaCO_3$ dissolution in acidic lysosomes, facilitate the disruption of lysosomes, and rapidly deliver DOX into the nuclei, demonstrating an in vivo antitumor effect against HeLa xenograft in mice.

Supplementary Information

The online version contains supplementary material available at https://doi.org/10.1186/s12645-023-00156-z.

Additional file 1: Figure S1. The reaction between PEI and CO_2 in water. Without water, two amino groups in PEI react with one CO_2 molecule forming alkylammonium carbamate zwitterions along the backbone. In the presence of water, some carbamate ions hydrolyze forming bicarbonate groups (shown in red). Water cannot improve CO_2 content in the final product. **Figure S2.** FTIR and ^{1}H NMR spectra of PEG-OTs and PEG-CHO. **Figure S3.** The XPS analysis of PEI-CO_2@$CaCO_3$-PEG-FA. (**A**) The survey scan showed the presence of C, N, O, and Ca elements. (**B**) High resolution of the C_{1S} scan displayed a major C=N(C–O) peak at 286.5 eV (from FA) and a C–C peak at 284.5 eV (from PEI and PEG) and C=O peak at 288 eV (from FA). (**C**) High resolution of the N_{1S} scan displayed a major C–N peak at 399 eV (from PEI and FA) and a minor C=N peak at 401 eV (from both FA and the Schiff base linkage between PEI backbone and PEG side chains). **Figure S4.** Particle morphology observation (**A**) and dynamic light scattering analyses (**B**) of the bare and DOX-loaded $CaCO_3$ nanoparticles. No obvious morphological change before and after DOX loading. Particle size measured by DLS increased while zeta potentials decreased. The PEG grafting further decreased the zeta potential. **Figure S5.** The Ca^{2+} release before (**A**) and after (**B**) loading of DOX. The loaded drug did not affect the release behavior. **Figure S6.** The CO_2 bubble formation from DOX/PEI@$CaCO_3$-PEG-FA (top) and DOX/PEI-CO_2@$CaCO_3$-PEG-FA (bottom). Both are stable at pH 7.4 but decompose at pH 6.5. More bubbles can be observed in the bottom right image. **Figure S7.** Cell endocytosis of FITC-labeled $CaCO_3$ nanoparticles. Green: $CaCO_3$ particles; blue: nuclei. More particles were endocytosed by HeLa cells. **Figure S8.** The internalized particles were encapsulated into lysosomes of L929 cells and released Ca^{2+} ions there. Green: $CaCO_3$ particles or Ca^{2+} ions; red: lysosomes; blue: nuclei. **Figure S9.** Histological observation of tumor sections after HE staining. The mice were treated with various nanoparticles for 14 d. A large area with very spare cell nuclei was found in the last two images, showing severe necrosis of tumor tissue in the two circumstances. **Figure S10.** Histological observation of various organ sections after HE staining. A tumor-like tissue was found in the liver from the saline group. Free DOX group demonstrated organic toxicity, showing small focal necrosis with infiltration of inflammatory cells in the heart, pyknosis and local necrosis in the liver, local necrosis in the spleen, thickened alveolar ducts in the lung, as well as glomeruli fusion with infiltration of inflammatory cells in the kidney. No pathological change was found in the organs from the other groups. **Figure S11.** FTIR spectra of PEI@$CaCO_3$ particles obtained from a colloidal aqueous solution that had been kept for up to 240 d at room temperature. The characteristic absorption at 745 cm^{-1} indicates the υ_4 CO_3^{2-} band (in-plane bending) that is typical for vaterite. For calcite, the band is at 712 cm^{-1}, which is absent in the spectra.

Declarations

Ethics approval and consent to participate

All animal experiments were approved by the Animal Ethics Committee of West China School of Pharmacy, Sichuan University, China.

Consent for publication

All authors consent for publication.

Competing interests

All authors declared no competing interests.

References

Agudelo D, Bourassa P, Bérubé G, Tajmir-Riahi HA (2016) Review on the binding of anticancer drug doxorubicin with DNA and tRNA: structural models and antitumor activity. J Photoch Photobio B 158:274–279

Balabushevich NG, Lopez De Guerenu AV, Feoktistova NA, Volodkin D (2015) Protein loading into porous $CaCO_3$ microspheres: adsorption equilibrium and bioactivity retention. Phys Chem Chem Phys 17:2523–2530

Binevski PV, Balabushevich NG, Uvarova VI, Vikulina AS, Volodkin D (2019) Biofriendly encapsulation of superoxide dismutase into vaterite $CaCO_3$ crystals. enzyme activity, release mechanism, and perspectives for ophthalmology. Colloids Surf B Biointerfaces 181:437–449

Boyjoo Y, Pareek VK, Liu J (2014) Synthesis of micro and nano-sized calcium carbonate particles and their applications. J Mater Chem A 2:14270–14288

Buscail L, Bournet B, Vernejoul F, Cambois G, Lulka H, Hanoun N, Dufresne M, Meulle A, Vignolle-Vidoni A, Ligat L, Laurent NS, Pont F, Dejean S, Gayral M, Martins F, Torrisani J, Barbey O, Gross F, Guimbaud R, Otal P, Lopez F, Tiraby G (2015) First-in-man phase 1 clinical trial of gene therapy for advanced pancreatic cancer: safety, biodistribution, and preliminary clinical findings. P Cordelier Mol Ther 23:779–789

Cao YQ, Zhang JS, Wang L, Cen MJ, Peng WC, Li Y, Zhang FB, Tan J, Fan XB (2021) Dual-functionalized covalent triazine framework nanosheets as hierarchical nonviral vectors for intracellular gene delivery. ACS Appl Nano Mater 4:4948–4955

Chen H, Kuang Y, Liu R, Chen ZY, Jiang BB, Sun ZG, Chen XQ, Li C (2018) Dual-pH-sensitive mesoporous silica nanoparticle-based drug delivery system for tumor-triggered intracellular drug release. J Mater Sci 53:10653–10665

Dizaj SM, Sharifi S, Ahmadian E, Eftekhari A, Adibkia K, Lotfipour F (2019) An update on calcium carbonate nanoparticles as cancer drug/gene delivery system. Expert Opin Drug Deliv 16:331–345

Dong Z, Feng L, Zhu W, Sun X, Gao M, Zhao H, Chao Y, Liu Z (2016) $CaCO_3$ nanoparticles as an ultra-sensitive tumor-pH-responsive nanoplatform enabling real-time drug release monitoring and cancer combination therapy. Biomaterials 110:60–70

Greenwald RB (2001) PEG drugs: an overview. J Control Release 74:159–171

Heathcote R, Howell JAS, Jennings N, Cartlidge D, Cobden L, Coles S, Hursthouse M (2007) Gold(I)–isocyanide and gold(I)–carbene complexes as substrates for the laser decoration of gold onto ceramic surfaces. Dalton Trans 13:1309–1315

Kalyane D, Raval N, Maheshwari R, Tambe V, Kalia K, Tekade RK (2019) Employment of enhanced permeability and retention effect (EPR): nanoparticle-based precision tools for targeting of therapeutic and diagnostic agent in cancer. Mater Sci Eng C 98:1252–1276

Kim SK, Foote MB, Huang L (2013) Targeted delivery of EV peptide to tumor cell cytoplasm using lipid coated calcium carbonate nanoparticles. Cancer Lett 334:311–318

Kircheis R, Wightman L, Wagner E (2001) Design and gene delivery activity of modified polyethylenimines. Adv Drug Deliv Rev 53:341–358

Min KH, Min HS, Lee HJ, Park DJ, Yhee JY, Kim K, Kwon IC, Jeong SY, Silvestre OF, Chen XY, Hwang YS, Kim EC, Lee SC (2015) pH-Controlled gas-generating mineralized nanoparticles: a theranostic agent for ultrasound imaging and therapy of cancers. ACS Nano 9:134–145

Morse JW, Arvidson RS, Lüttge A (2007) Calcium carbonate formation and dissolution. Chem Rev 107:342–381

Pandey AP, Sawant KK (2016) Polyethylenimine: a versatile, multifunctional non-viral vector for nucleic acid delivery. Mater Sci Eng C 68:904–918

Park HK, Lee I, Kim K (2004) Controlled growth of calcium carbonate by poly(ethylenimine) at the air/water interface. Chem Commun 1:24–25

Popova V, Poletaeva Y, Pyshnaya I, Pyshnyi D, Dmitrienko E (2021) Designing pH-dependent systems based on nanoscale calcium carbonate for the delivery of an antitumor drug. Nanomaterials 11:2794

Shen X, Du H, Mullins R, Kommalapati R (2017) Polyethylenimine applications in CO_2 capture and separation: from theoretical study to experimental work. Energy Technol 5:822–833

Shi JJ, Zhang HL, Wang L, Li LL, Wang HH, Wang ZZ, Li Z, Chen CQ, Hou L, Zhang CF, Zhang ZZ (2012) PEI-derivatized fullerene drug delivery using folate as a homing device targeting to tumor. Biomaterials 34:251–261

Som A, Raliya R, Tian LM, Akers W, Ippolito JE, Singamaneni S, Biswas P, Achilefu S (2016) Monodispersed calcium carbonate nanoparticles modulate local pH and inhibit tumor growth in vivo. Nanoscale 8:12639–12647

Sun QH, Sun XR, Ma XP, Zhou ZX, Jin EL, Zhang B, Shen YQ, Van Kirk EA, Murdoch WJ, Lott JR, Lodge TP, Radosz M, Zhao YL (2014) Integration of nanoassembly functions for an effective delivery cascade for cancer drugs. Adv Mater 26:7615–7621

Sun QH, Zhou ZX, Qiu NS, Shen YQ (2017) Rational design of cancer nanomedicine: nanoproperty integration and synchronization. Adv Mater 29:1606628

Trushina DB, Bukreeva TV, Kovalchuk MV, Antipina MN (2014) $CaCO_3$ vaterite microparticles for biomedical and personal care applications. Mater Sci Eng C 45:644–658

Trushina DB, Borodina TN, Belyakov S, Antipina MN (2022) Calcium carbonate vaterite particles for drug delivery: advances and challenges. Mater Today Adv 14:100214

Unger RE, Stojanovic S, Besch L, Alkildani S, Schröder R, Jung O, Bogram C, Görke O, Najman S, Tremel W, Barbeck M (2022) *In vivo* biocompatibility investigation of an injectable calcium carbonate (vaterite) as a bone substitute including compositional analysis via SEM-EDX technology. Int J Mol Sci 23:1196

Vikulina A, Voronin DV, Fakhrullin RF, Vinokurov VA, Volodkin D (2020) Naturally derived nano- and micro-drug delivery vehicles: halloysite, vaterite and nanocellulose. New J Chem 44:5638–5655

Volodkin DV, Petrov AI, Prevot M, Sukhorukov GB (2004) Matrix polyelectrolyte microcapsules: new system for macromolecule encapsulation. Langmuir 20:3398–3406

Wang S, Low PS (1998) Folate-mediated targeting of antineoplastic drugs, imaging agents, and nucleic acids to cancer cells. J Control Release 53:39–48

Wang S, Ni DZ, Yue H, Luo NN, Xi XB, Wang YG, Shi M, Wei W, Ma GH (2018) Exploration of antigen induced $CaCO_3$ nanoparticles for therapeutic vaccine. Small 14:1704272

Xu M, Zhang J, Mu Y, Foda MF, Han H (2022) Activation of TRPV1 by capsaicin-loaded $CaCO_3$ nanoparticle for tumor-specific therapy. Biomaterials 284:121520

Yang T, Wan Z, Liu Z, Li H, Wang H, Lu N, Chen Z, Mei X, Ren X (2016) *In situ* mineralization of anticancer drug into calcium carbonate monodisperse nanospheres and their pH-responsive release property. Mater Sci Eng C 63:384–392

Zhao Y, Luo Z, Li M, Qu Q, Ma X, Yu SH, Zhao Y (2015) A preloaded amorphous calcium carbonate/doxorubicin@silica nanoreactor for pH-responsive delivery of an anticancer drug. Angew Chem Int Ed 54:919–922

Zhu L, Shi Y, Tu C, Wang R, Pang Y, Qiu F, Zhu X, Yan D, He L, Jin C, Zhu B (2010) Construction and application of a pH-sensitive nanoreactor via a double-hydrophilic multiarm hyperbranched polymer. Langmuir 26:8875–8881

Publisher's Note

Springer Nature remains neutral with regard to jurisdictional claims in published maps and institutional affiliations.